RESEARCH ARTICLE OPEN ACCESS

Comparative Fatigue Analysis of Structural Steels Considering Welding and Surface Effects

Yevgen Gorash[1] | Tugrul Comlekci[1] | Carl Walker[2] | Athanasios Toumpis[3] | James Kelly[3] | Andrew England[1] | Lewis Milne[1]

[1]Weir Advanced Research Centre, University of Strathclyde, Glasgow, UK | [2]Divisional Technology, Weir Minerals Australia, Artarmon, Australia | [3]Mechanical and Aerospace Engineering, University of Strathclyde, Glasgow, UK

Correspondence: Yevgen Gorash (yevgen.gorash@strath.ac.uk)

ABSTRACT

There are limited data on the very high-cycle fatigue for structural steel welds for over 10 million cycles. The purpose of this research is a fatigue performance comparison of the welds made of steels S355JR+AR and S275JR+AR. The goal of reaching the gigacycle fatigue domain is achieved using the ultrasonic fatigue testing at 20 kHz. Fatigue samples are prepared to investigate the influence of two surface conditions—polished and precorroded. Fatigue failures are driven primarily by welding porosity with the fatigue life duration dependent on the size and location of pores. Visual comparison of fatigue data for steels poses a challenge, because of the vast scatter of experimental data points. Therefore, a statistical approach is used with a fatigue performance parameter applied to the fatigue data for welded samples to quantify the quality of the structural materials.

1 | Introduction and Motivation

Unalloyed low-carbon steel grades S235, S275 and S355, according to EN 10025 [1], are common structural materials for the heavy machinery in minerals and sand-and-aggregate applications. Currently, these components are designed with high safety factors against SN curves with an assumed asymptotic fatigue limit above $> 10^7$ load cycles. Nevertheless, fatigue cracks are seen even at the high number of cycles ($> 10^8$), producing a big data scatter (over an order of magnitude) as the stress reduces. While high-cycle fatigue failure occurs at the surface, fatigue cracks at the very high number of cycles ($> 10^8$) may initiate at oxides or intermetallic inclusions below the surface (or slag and flux inclusions for welds) typical for very high-cycle fatigue (VHCF) regime. Recently, ultrasonic fatigue (USF) testing results have been published for S275JR+AR steel [2] and for Q355B steel [3] that demonstrated

a pronounced frequency effect and several technical challenges associated with accelerated fatigue testing. However, there is almost no VHCF data ($> 10^8$) for the welds made of low-carbon steel grades from EN 10025 [1] and their equivalents with a very limited number of publications up to date, which are discussed below. So this research is focused on USF testing of two specific subgrades S275JR+AR and S355JR+AR with a goal of fatigue performance comparison. The fatigue welded samples are prepared with two surface conditions (polished and precorroded) to investigate the extent of damage induced by the surface effect. The main purpose of this research is a fatigue performance comparison of the welds made of currently preferred steel S355JR+AR and the candidate steel S275JR+AR. Welded heavy machinery assemblies are designed to work for several years of guaranteed service life at typically 15- to 20-Hz frequencies of loading under low stress amplitudes. In order to reach a few billion cycles within

---

Abbreviations: FPP, fatigue performance parameter; HAZ, heat-affected zone; s/s, subsurface; USF, ultrasonic fatigue; VHCF, very high-cycle fatigue.

a practically sustainable testing time, an accelerated fatigue testing method is required. The goal of reaching the gigacycle fatigue domain is achieved using the USF testing approach with Shimadzu USF-2000A system [4].

2 | VHCF of Welds

The fatigue properties of structural steels in the VHCF regime has attracted attention in research due to their use in applications such as civil infrastructure [5]. The VHCF behaviour of two subgrades (J0 and J2) of S355 structural steel was characterised by Klusàk et al. [5], who observed failures for both subgrades over 10^{10} cycles. It was found that there was no difference in the fatigue behaviour of each subgrade or for the specimen orientation with respect to the rolling direction. Cracks mainly initiated from the surface, but internal fractures which initiated from non-metallic inclusions were also identified [5]. A similar fatigue behaviour was observed by Swacha and Lipski [6] for S355J2 structural steel. USF testing is well known to have an effect on the fatigue strength of ferritic–pearlitic structural steels and has been demonstrated for a range of grades [3, 7–9]. Guennec et al. [10] proposed a model, based on dislocation energy theory, to relate the fatigue endurance to test frequency and wt.% C for structural steels. The model was demonstrated to be applicable for structural steels with a wide range of wt.% C [10].

Standards for fatigue design of welded structures assume that the SN curves reach an asymptotic fatigue limit at a certain number of cycles, for example, 10^7 cycles in BS7608 [11]. This raises an issue when considering the design of structures with service lives in the VHCF domain [12]. It has been demonstrated through USF testing that fatigue failures of welds can occur beyond 10^7 stress cycles [13–18]. The failure of welded joints in the VHCF domain has also been observed for in-service components [19–21]. Fry [19] showed that failures of welded beams on vibrating screens occur beyond 10^8 stress cycles and proposed an extension to the SN curves in BS7608 [11] for heavy industry equipment cyclically loaded to the VHCF domain.

The VHCF properties of structural steel welds have been investigated by a few researchers due to their use in applications where $> 10^7$ stress cycles are experienced, for example, bridges, off-shore structures and railway components [15, 17]. Conventional specimens with a cylindrical hourglass shape and a polished surface are typically used for USF testing of structural steel parent metals. The specimen geometries employed for welds are more diverse, with examples including cylindrical dog bone [22], as-welded butt joints [23] and cruciform joints [14].

Zhao et al. [13] studied the VHCF performance of EH36 using smooth cylindrical hourglass specimens and observed no fatigue limit for both the base metal and welded joint, with failures occurring above 10^9 cycles. It was also found that the fatigue strength of the base metal was greater than the welded joint, especially as the numbers of cycles to failure increased. This was attributed to the presence of gas pore and inclusion type defects in the welded specimens that fatigue cracks

initiated from [13]. A similar trend in a reduction in fatigue strength due to defects was observed for Q345 structural steel welded joints with cracks originating at slag inclusions, gas pores and lack of fusion defects in cylindrical hourglass specimens [15]. Butt joints of 16Mn structural steel were examined by Liu et al. [16] in the as-welded condition using USF testing. It was observed that the welded joints had a reduced fatigue strength compared to the base metal and that fatigue cracks generally originated from the weld toe or stop–start region due to the stress concentration these produced [16]. The VHCF behaviour of Q345 welds was investigated by He et al. [17], who designed a semicircular notched specimen to discretely evaluate the fatigue strength of the base metal, heat-affected zone (HAZ) and fusion zone (FZ). All regions showed a continually decreasing SN curve in the VHCF domain and the HAZ and FZ displayed significantly reduced fatigue strength compared to the base metal [17]. The VHCF behaviour of Q345 welds under multiaxial loading was investigated using cruciform specimens by Xue et al. [24]. The fatigue strength under biaxial loading was reduced by approximately 55% compared to uniaxial loading and fatigue cracks initiated from pores and lack of fusion defects [24].

In addition to the structural steels detailed above, alloy steels are another class of materials that have received some attention in research. The frequency and size effects associated with USF testing were investigated by Zhu et al. [25, 26] using cylindrical dog-bone Cr-Ni-Mo-V steel welded specimens. Tests conducted at 20 kHz showed a notable increase in fatigue strength when compared to tests conducted at 110 Hz, confirming the frequency effect commonly observed with base metals [2, 3, 10] remains an issue with welds [25]. It was also found that as the specimen diameter was increased, the fatigue strength decreased due to the increased probability of a critical defect serving as a crack initiation site [26]. The thermal dissipation during USF testing of welded joints, a challenge identified during testing of base metals [27], was assessed by Hu et al. [28]. Using the same welded joint as described above [25, 26], a significant increase in specimen surface temperature was observed, especially during the crack propagation period [28]. Yeom et al. [29] found that welding resulted in only a minimal decrease in VHCF strength of 590 FB and 780 FB steel flat dog-bone specimens, in contrast to other research comparing welded joints to base metals [13, 16, 17, 30]. Welded joints of KMN-I alloy steel exhibited failures in the VHCF domain from internal matrix crack initiation in cylindrical hourglass specimens [30]. There is also limited research on the VHCF behaviour of stainless-steel welds, with fatigue failures observed above 10^7 stress cycles for welds of 316L [31] and FV520B-I [22, 32].

The influence of defects on VHCF behaviour of welds has also been observed for electron beam welded TC17 titanium alloy [33]. A large scatter was observed in the fatigue results of cylindrical hourglass specimens due to the random distribution of pore size and the distance from the pore to the specimen surface [33]. Additionally, Xiong et al. [31] found a similar dependence between the pore distribution and VHCF behaviour for cylindrical hourglass specimens of 316L stainless steel joined using laser beam welding. A greater scatter in fatigue lives was observed for laser beam welded joints when compared to 316L weldments fabricated by gas tungsten arc welding [31].

3 | Experimental Procedures

3.1 | Ultrasonic (US) Machine

The number of cycles beyond 10^7 can be attained in a viable period using the recently developed high-frequency testing machines, which typically run at 20 kHz. Evaluating the VHCF behaviour of materials is becoming increasingly important for applications such as mineral separation and transportation. As equipment in these sectors is required to last for years or even decades of continuous service, the number of load cycles they must withstand without failure will easily reach into the gigacycle domain ($> 10^9$ cycles). To assess fatigue for 10^9 cycles requires 1.6 years of normal testing at 20 Hz, which is not feasible. In contrast to that, when doing USF testing at 20 kHz, it would take only 0.6 days if intensive cooling is not required. Therefore, the central piece of the experimental setup is an USF testing system with a mean stress loading mechanism consisting of a standard Shimadzu USF-2000A machine and Shimadzu AG-X series (AG-X5kN) table-top autograph by Japanese company Shimadzu Corp. [4], with a maximum of 5-kN tensile load. Mean stress loading was applied to the 20-kHz samples using the AG-X5kN, which exerts a constant mean stress in the test sample by pulling it from both ends with the recommended force of ≤ 1.5 kN. The central piece, USF-2000A machine, is attached to the moving crosshead on one side and the frame base on the other side with a test sample in the middle. The air-cooling nozzles are pointed at the sample to suppress its intensive heating [27] caused by internal heat dissipation at around the resonance frequency of 20 kHz. The

USF testing method implemented in Shimadzu USF-2000A machine was standardised by the Japan Welding Engineering Society [34, 35]. This standard provides requirements for apparatus, specimens, test procedures, stress calculation methods and other necessary items. The data analysis carried out in the process of writing the standard [34, 35] suggests that the USF testing is well suited to high-strength materials but not low-strength materials, which highlights the significant challenge in USF testing of structural steels, including grades S275 and S355 [2].

3.2 | Tensile Testing

USF testing is based on the resonance loading by inducing longitudinal elastic waves in the specimen, with a peak in its central gauge location. Therefore, a proper setup of the US test and proper design of the corresponding specimen require accurate elastic properties of the tested material (Young's modulus E and Poisson's ratio ν) and density ρ, as these properties directly define the stress amplitude and mean stress values applied to the sample. The values of Poisson's ratio $\nu = 0.3$ in elastic range and density $\rho = 7850$ kg/m^3 take been taken from the standard EN 1993-1-1 [36], as they would have a negligible variation for a 12- to 15-mm-thick steel plate. Other mechanical properties (Young's modulus E, 0.2% proof stress $\sigma_{0.2\%}$, ultimate tensile strength, elongation at break L^*) derived from the stress–strain curve were evaluated by carrying out tensile tests using an Instron 8802 servo-hydraulic fatigue testing system with an actuator force capacity of up to ± 250 kN.
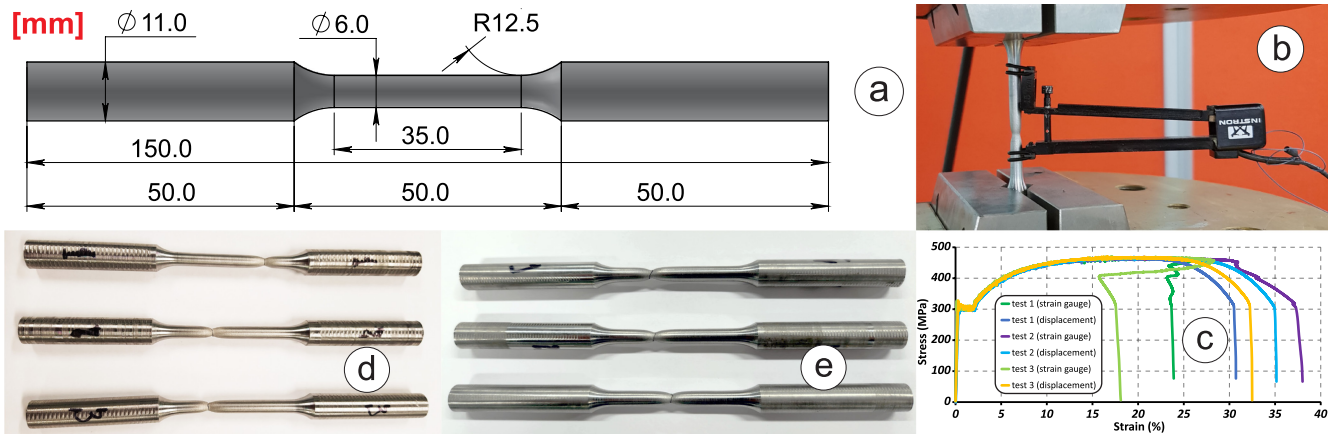
FIGURE 1 | Validating mechanical properties of S275JR+AR and S3555JR+AR steels via tensile testing with corresponding results in Table 1: (a) dimensions of the specimen (mm), (b) specimen with a clip-on extensometer attached, (c) stress–strain curves for S275JR+AR, (d) necking at failure for S275JR+AR and (e) necking at failure for S355JR+AR.

TABLE 1 | Mechanical properties of hot-rolled plates made of S275JR+AR and S355JR+AR structural steels derived from stress–strain curves.

Steel grade	Plate thickness	Young's modulus (GPa)	0.2% proof stress (MPa)	Tensile strength (MPa)	Elongation at break (%)
S275JR+AR	12 mm	211.1/210[c]	314/338[a]/275[b]	468.9/469[a]/410[b]	31.8/30.5[a]/23[b]
S355JR+AR	15 mm	210.7/210[c]	378.2/405[a]/355[b]	512.8/512[a]/470[b]	24.3/24.0[a]/22[b]

[a]From the material quality certificates provided by manufacturers.
[b]According to the standard EN 10025-2 [1].
[c]According to the standard EN 1993-1-1 [36].

Round tensile specimens 150 mm long were cut from the hot-rolled plate with a thickness of 12 mm, as shown in Figure 1a. The grip length sides are both 50 mm long—selected in order to provide the most reliable grip of the sample by the hydraulic grippers. The gauge length is 35 mm, which marks the distance between the fillets of radius $R = 12.5$ mm—selected to accommodate the available clip-on extensometer. The gauge diameter of the tensile specimens is $D_g = 6$ mm. The cylindrical shape of samples and the ratio of grip diameter to gauge diameter 1.83 have been adopted according to the available source material and recommendations of ASTM E466-21 [37] standard, which implies that the grip diameter should be approximately 1.22 times, but preferably 2 times, the gauge diameter. Strain was recorded using two methods: (a) clip-on extensometer attached to the sample using rubber O-rings as shown in Figure 1b and (b) force–displacement response as shown in Figure 1c converted into stress and strain. Three specimens were tested for each steel until failure with a loading rate of 1 mm/min with the stress–strain curves.

The obtained experimental values for both grades were averaged and reported in Table 1 and compared to the values from the material quality certificates provided by the manufacturer and values from standards EN 10025-2 [1] and EN 1993-1-1 [36]. The comparison indicates following:

- slight deviation of Young's modulus from the standard $E = 210$ GPa from EN 1993-1-1 [36];

- slightly better values of 0.2% proof stress $\sigma_{0.2\%}$ in the certificates compared to the averaged values from experiments;

- perfect match of the experimental values of UTS σ_u and elongation at break L^* to the certificate and much better than the standard EN 10025-2 [1] values.

However, both yield/tensile strengths and elongation at break of the actual materials are superior to those minimum values prescribed by the standard EN 10025-2 [1].

It should be noted that all the samples for S275JR+AR steel testing were cut from a single hot-rolled plate sized 1×2 m produced by 'Ilyich Iron and Steel Works' (Mariupol, Ukraine) in May 2019—Cast No. 293262-2, Batch No. 20540. All the samples for S355JR+AR steel testing were cut from a single hot-rolled plate sized 1×2 m produced by the steel and mining company 'Severstal' (Cherepovets, Russia) in May 2020—Cast No. 103152, Batch No. 4085501.

3.3 | Conventional Fatigue Testing

Low-frequency testing 15–20 Hz was done in the range of stress amplitudes $\sigma_a \in 200{-}275$ MPa for the stress ratio $R = -1$. The specimen geometry was the same as was in tensile testing, but with a better ('mirror') surface finish of $R_a = 0.8$ μm—round tensile specimens 150-mm-long cut from the hot-rolled plate with a thickness of 12 mm, as shown in Figure 1a. Data points were obtained using two servo-hydraulic fatigue testing systems—at 15 Hz with 150-kN frame Instron 8801 and at 20 Hz with 250-kN frame Instron 8802. The summary of the obtained fatigue testing results for S275JR+AR and S355JR+AR grades is shown in Figure 2 in the form of experimental data points and corresponding fitted SN curves. The obtained SN curves using least squares regression shows little scatter with $R^2 = 0.92$ for S275JR+AR steel and larger scatter with $R^2 = 0.60$ for S355JR+AR steel, as can be observed in Figure 2. These SN curves look non-conservative when comparing the fatigue limits to the available 'design' SN curves from material databases GRANTA [38] and FKM [39]. Both SN curves for S275JR+AR and S355JR+AR grades look better than the lower bound of the collected fatigue data band for JR, J0 and J2 subgrades of S275J and S355J from the Granta database [38] but worse than the synthetic 97.5% probability SN curves for S275JR and S355JR subgrades from the FKM database [39]. The SN curves in Figure 2 are fitted to the experimental data using least squares regression and the classical Basquin's equation [40] that describes high-cycle and very high-cycle low-strain behaviour:
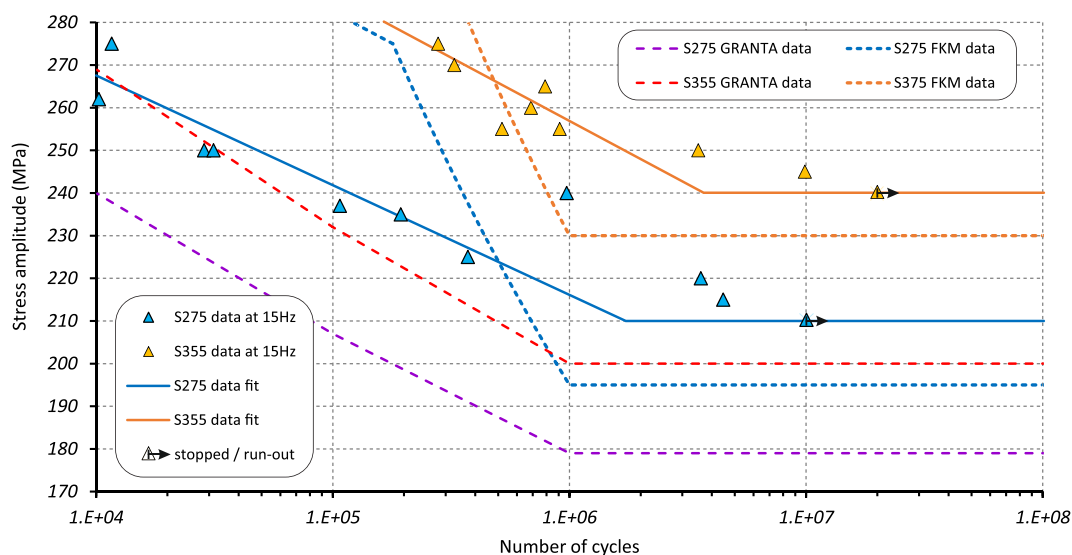
FIGURE 2 | Conventional SN curves for S275JR+AR and S355JR+AR grades obtained at normal frequency 15-20 Hz compared to design SN curves from GRANTA [38] and FKM [39] databases.

$$\sigma_a = \frac{\Delta\varepsilon_e}{2} E = \sigma'_f (2N)^b, \tag{1}$$

where σ_a is the amplitude of alternating stress; E is Young's modulus; N is the number of cycles to failure and $2N$ is the number of reversals to failure; b is a fatigue strength exponent, for common metals $-0.12 < b < -0.05$; and σ'_f is a fatigue strength coefficient, which is approximately equal to the monotonic true fracture stress σ_f. Corresponding values of the fatigue material parameters (b and σ'_f) and the values of coefficients of determination (R^2) are reported in Table 2 for both experimental SN curves and SN curves from material databases [38, 39]. It should be noted that σ_f values not far away from tensile strength are reported in Table 1.

The conventional fatigue limit at low frequency for S275JR+AR is expected to be around 210 MPa, which is higher than the values of 179 MPa from GRANTA [38] and 195 MPa from FKM [39]. The conventional fatigue limit at low frequency for S355JR+AR is expected to be around 240 MPa, which is higher than the values of 200 MPa from GRANTA [38] and 230 MPa from FKM [39]. It should be noted that the obtained fatigue limit of 210 MPa for S275JR+AR is confirmed at 10 million cycles and 240 MPa for S355JR+AR is confirmed at 20 million cycles, which are quite different to the fatigue limits from the material databases [38, 39], which are only confirmed at 1 million cycles.

4 | Welded Specimens

4.1 | Manufacturing of Welded Specimens

The USF samples for welds testing have a standard tapered shape geometry as shown in Figure A1 of Appendix A—exactly the same as used in testing of S275JR+AR parent material in the preceding work [2]. Preparation of these axisymmetrical samples requires cutting of 20 rectangular blanks (12×12 mm in cross-section) for S275JR+AR as shown in Figure A2a of Appendix A and 25 blanks (15×15 mm in cross-section) for S355JR+AR as shown in Figure A3a of Appendix A. Blanks are 160 mm long and cut out of the welded plates using water-jet cutter to have a HAZ in the middle as shown in Figures A2b and A3b of Appendix A. The obtained blanks are turned into the axisymmetrical samples as shown in Figure A1 using HAAS TL-1 CNC Lathe. Two plates sized as 200×400 mm with a thickness of 12 or 15 mm were welded with a double-V butt joint using metal inert gas (MIG) welding process to produce a 400×400 mm

square plate. MIG is an arc welding process that uses a continuous solid wire electrode heated and fed into the weld pool from a welding gun. The two base materials are melted together forming a joint. The gun feeds a shielding gas alongside the electrode helping protect the weld pool from airborne contaminants. The most important requirements to this particular welding are the following:

- butt weld preparation angle is 30° or corresponding groove angle is 60° (see Figures A2c and A3c of Appendix A);

- the root gap between the plates is 2 mm with root face length of 3 mm (see Figures A2c and A3c of Appendix A);

- 1.2-mm copper-coated MIG wire according to ER70S-6 AWS A5.18 specification;

- shielding gas composition: 95% Ar, 3% CO_2, 2% O_2;

- radiographic (X-ray) and US inspections of welds confirmed the perfect fusion and absence of cracks;

- mandatory postweld heat treatment (PWHT), that comprised heating with rate of 150°C/h, than holding at 600°C for 1 h, followed by cooing with the rate 150°C/h for 2 h down to 400°C and final cooling in still air as shown in Figure A4.

4.2 | Inspection of Welds Quality

All plates were welded manually at the welding facility of Doosan Babcock Ltd by an expert welder with corresponding Welding Procedure Qualification Records (WPQR) and radiographic (X-ray) and US inspection reports provided for each welded plate. According to WPQR for S275JR+AR grade, a produced weld consists of seven passes in total, as shown in Figure 3a. According to WPQR for S355JR+AR grade, a produced weld consists of 9 passes in total, as shown in Figure 3b. The preheating was not required as the plates are relatively thin. The first pass is applied to the root in the middle of the plate, and then, the second pass completes the welding of one plate side, as can be confirmed by the microstructure image in Figure A5a for the weld cross-section extracted from Plate ID No. ZL805 made of S275JR+AR grade and Figure A6a for the weld cross-section extracted from Plate ID No. ZL781 made of S355JR+AR grade. Before performing the welding of the opposite side, its groove is ground and wire brushed. Another five passes are deposited on the opposite side of S275JR+AR plate according to the schematics in Figure 3a and confirmed by the micrograph shown in

TABLE 2 | Material parameters of SN curves presented by Equation (1) shown in Figure 2.

Parameters	Experimental		FKM [39] (HCF range)		FKM [39] (LCF range)		GRANTA [38]	
	S275JR+AR	S355JR+AR	S275JR	S355JR	S275JR	S355JR	All S275J	All S355J
b	−0.047	−0.049	−0.2	−0.2	−0.037	−0.031	−0.064	−0.064
σ'_f (MPa)	426.15	520.92	3550.1	4187.4	441.2	521.1	453.4	508.2
R^2	0.92	0.60	n/a	n/a	n/a	n/a	n/a	n/a
σ_{lim} (MPa)	210	240	195	230	195	230	179	200

Figure A5a of Appendix B. Another seven passes are deposited on the opposite side of S355JR+AR plate according to the schematics in Figure 3b and confirmed by the micrograph shown in Figure A6a of Appendix B.

Welds in both plates (ID No. ZL805 and No. ZL781) were tested for Vickers low-force hardness with a hardness number of $HV = 0.5$ using Mitutoyo MVK G1 microhardness tester. The hardness measurements were taken at the weld cross-section along three different paths (top, middle and bottom) consisting of 52 points each as shown in Figure A5a for S275JR+AR weld and Figure A6a for S355JR+AR weld. The average Vickers hardness is 155 $HV0.5$ for S275JR+AR weld and 178 $HV0.5$ for S355JR+AR weld as reported in Table 3 together with mean, range, min. and max. values for top, middle and bottom paths shown in Figures A5b and A6b correspondingly. The spikes in hardness are visible on all three patches with over 190 for S275JR+AR weld and over 220 for S355JR+AR weld at the locations corresponding to HAZ paths.

These results for both grades show that the hardness of the HAZ is much higher than that of the base metal and slightly higher than that of the weld metal. Increased hardness of HAZ is usually associated with the bainite formation within HAZ 1. Both coarse-grained and fine-grained microstructures of HAZ can be easily seen in Figures A5a and A6a of Appendix B. HAZ 1 (coarse-grained HAZ) immediately adjacent to the weld pool has achieved austenite temperature (~850°C–1500°C melting point) and can form bainite or martensite depending on cooling rate. HAZ 1 undergoes the most extreme heating and cooling rates due to its proximity with the weld pool. HAZ 2 (fine-grained HAZ) typically shows grain refinement and modified pearlite due to this zone achieving subcritical or intercritical temperature (~700°C–850°C). Stress relief, recrystallisation and carbon diffusion occur within HAZ 2, which is normally the least affected and can give hardness values similar to the unaffected parent material.

Both radiographic (X-ray) and US inspections of welds has been conducted with all welded plates with an acceptance criteria according to the standard ISO 5817 [41]. The purpose of US inspection is to detect the lack of fusion, while the purpose of X-ray inspection is to investigate the extent of welding porosity considering both size and concentration of pores. The X-ray inspection revealed an absolutely random distribution of welding pores with a variation from frequent small pores of 50–100 μm in diameter to very rare and occasional big pores up to almost 1 mm in diameter. The random character of pore distribution and size can be observed on a corresponding X-ray image for Plate ID No. ZL805 in Figure 4 for S275JR+AR and Figure 5 for S355JR+AR. So it was not really practically possible to separate pore-free samples from the complete batch of samples based on X-ray images, because of this randomness.

5 | Analysis of Results

5.1 | Parent Metals

USF testing of S275JR+AR grade in parent condition is covered comprehensively in the preceding work [2]. In addition to USF material parameters for S275JR+AR, this paper reports SN curves, corresponding material parameters and the 'high strain-rate' fatigue limit for polished samples of S355JR+AR steel in parent condition. All testing was implemented using Shimadzu USF-2000A machine using tapered USF samples with a standard shape and a finer 'mirror' surface finish of $R_a = 0.8$ μm as shown in Figure A1 of Appendix A at 20 kHz under zero mean stress condition $R = -1$ with a run-out at 10 billion cycles. It is
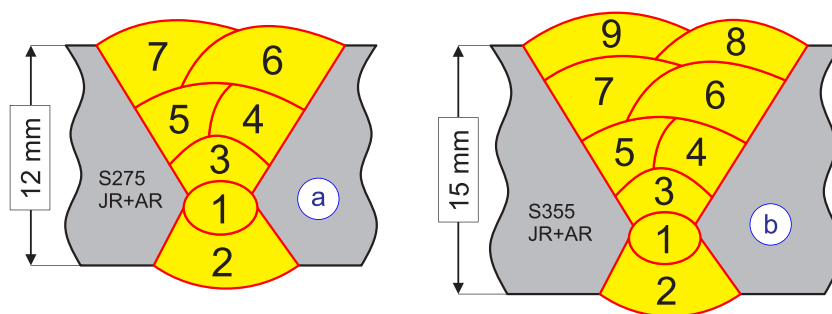
FIGURE 3 | The sequence of passes for the welded plates made of (a) S275JR+AR and (b) S355JR+AR.

TABLE 3 | Statistics of Vickers hardness $HV0.5$ measured in weldments.

Grades	S275JR+AR			S355JR+AR		
Average		155			178	
Path	Top	Middle	Bottom	Top	Middle	Bottom
Mean	155.25	140.23	150.65	178.23	171.71	178.44
Range	63	44	84	80	91	59
Min.	129	122	122	152	152	156
Max.	192	166	206	232	243	215
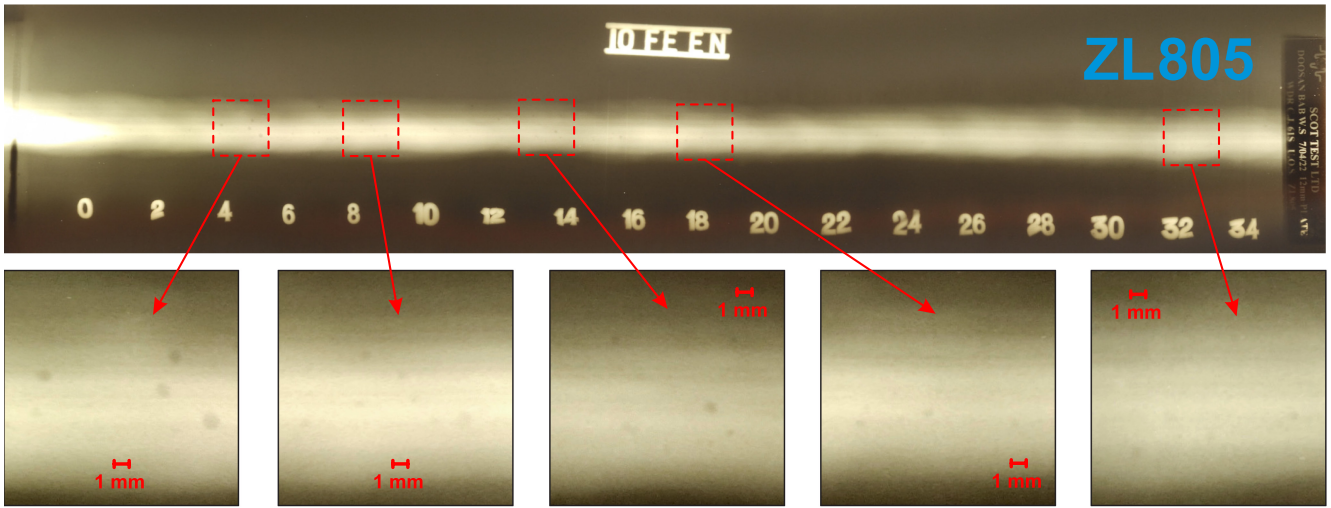
FIGURE 4 | X-ray image of the 400-mm-long welds joining S275JR+AR Plate ID No. ZL805 with closer views of bigger pores.
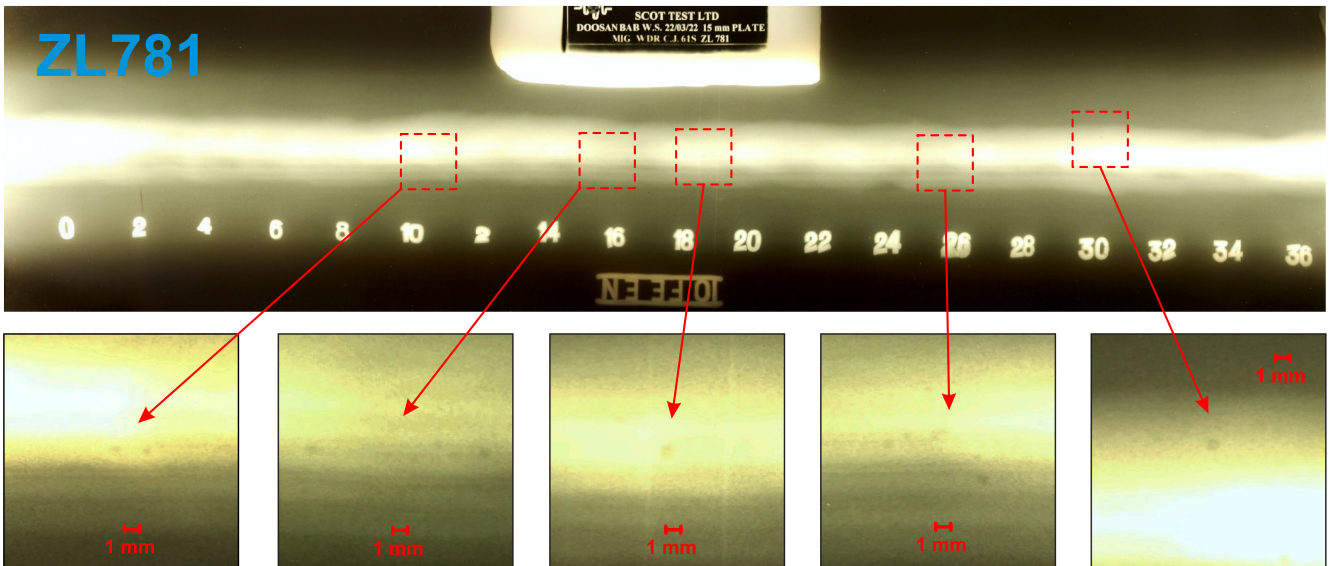
FIGURE 5 | X-ray image of the 400-mm-long welds joining S355JR+AR Plate ID No. ZL781 with closer views of bigger pores.

TABLE 4 | Material parameters of the USF SN curves using Equation (1) for parent metals for the least squares regression lines shown in Figures 6 and 7.

Grades	S275JR+AR		S355JR+AR	
USF σ_{lim}	340 MPa		370 MPa	
Parameters	Surface	Subsurface (s/s)	Surface	Subsurface (s/s)
b	−0.03	−0.031	−0.024	−0.024
σ_f' (MPa)	599.71	659.12	576.77	645.65
R^2	0.93	0.98	0.88	n/a

assumed that a crack may originate from the sample surface—a typical for HCF with a majority of samples failing this way. But also a crack may originate from very close to the surface or subsurface (s/s) with a significant delay in number of cycles (one order of magnitude for S275JR+AR and two orders of magnitude for S355JR+AR)—a typical fracture mechanism for VHCF with just a few samples failing this way. The SN curves are fitted to the experimental data using least squares regression and
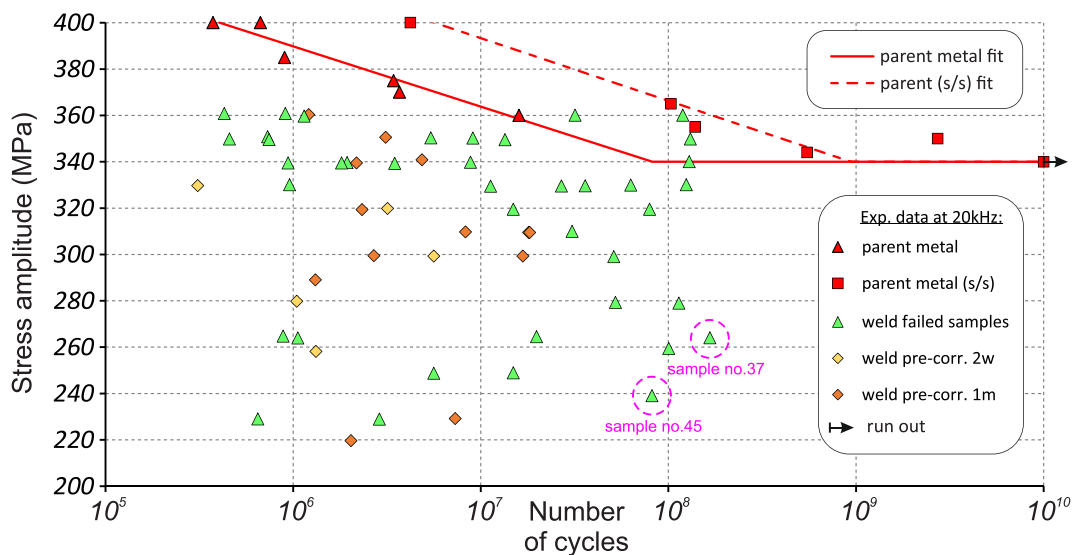
FIGURE 6 | Summary of USF testing for S275JR+AR weldments with polished and precorroded surface compared to parent material results.
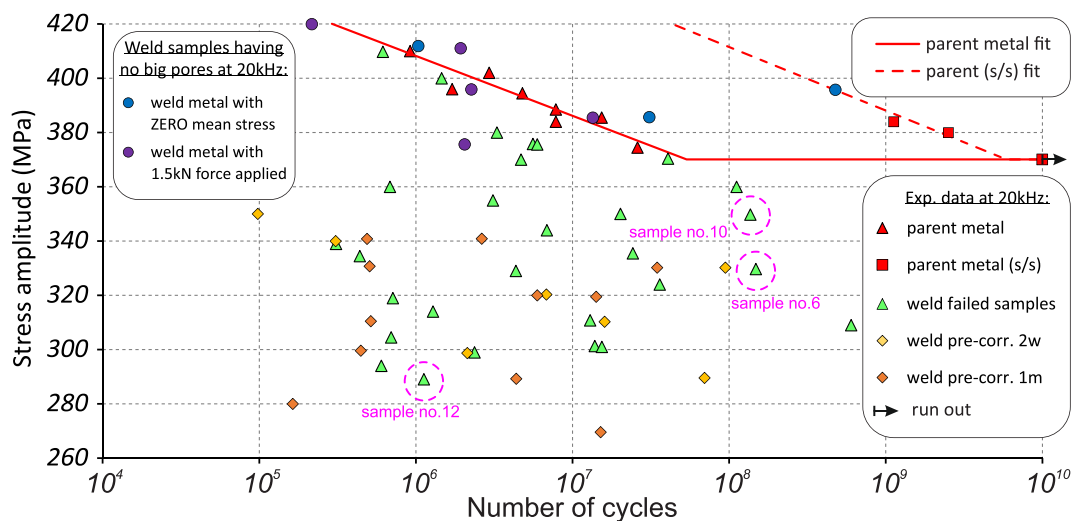
FIGURE 7 | Summary of USF testing for S355JR+AR weldments with polished and precorroded surface compared to parent material results.

the classical Basquin's equation [40] (1) explained in Section 3.3 with the fatigue material parameters—b as a fatigue strength exponent and σ_f' as a fatigue strength coefficient. As a result of fitting, four groups of material parameters (b and σ_f') are identified and reported in Table 4—for two grades (S275JR+AR and S355JR+AR) and two failure modes (HCF and VHCF)—together with the values of the coefficient of determination (R^2) and the USF limit σ_{lim}.

Parent metal data for S275JR+AR and S355JR+AR grades are shown in Figures 6 and 7 correspondingly in the form of SN curves for surface and s/s fitted to the experimental data points. Both groups of data points for S275JR+AR parent metal demonstrate a relatively small scatter ($R^2 = 0.93$ and $R^2 = 0.98$ for surface and s/s, respectively, from Table 4) when fitted with least squares regression. The surface group of S355JR+AR parent metal demonstrates higher scatter ($R^2 = 0.88$ from Table 4) compared to S275JR+AR ($R^2 = 0.93$ and $R^2 = 0.98$ for surface and s/s, respectively). This observation agrees perfectly with a similar comparison of the conventional fatigue

data obtained at low frequency in Table 2, where the fitting accuracy for S275JR+AR steel ($R^2 = 0.92$) is much higher than for S355JR+AR steel ($R^2 = 0.60$). As the s/s group of S355JR+AR parent metal consist of only 2 data points, the same fatigue strength exponent b is used as for the surface group, providing visually acceptable fitting accuracy, as can be seen in Figure 7.

The USF limit for S275JR+AR parent metal is found to be 340 MPa, as confirmed by the specimen that ran out after 10 billion cycles. The stress amplitude value of $\sigma_{lim} = 340$ MPa was reached at 8.21×10^7 cycles when extrapolating the SN curve with a crack originating on the surface or at 9.39×10^8 cycles when extrapolating the SN curve with a crack starting from very close to the surface or s/s, as shown in Figure 6. It can therefore be assumed that fatigue failure for S275JR+AR parent metal is unlikely when the stress is below 340 MPa and over 1 billion cycles have been accumulated. In the existing experimental batch of S275JR+AR parent metal, five samples were found as outliers, as they demonstrated an order of magnitude longer fatigue life

compared to the primary group (surface crack). The crack initiation process was significantly delayed in those samples, and for this reason, they have been grouped into a secondary s/s group and used to generate a s/s SN curve in Figure 6. This division of USF fatigue data into two groups (surface and s/s) was discussed in previous work [2] focussed on parent material providing references, both optical and SEM microscopy with corresponding images.

The USF limit for S355JR+AR parent metal is found to be 370 MPa, as confirmed by the specimen that ran out after 10 billion cycles. The stress amplitude value of $\sigma_{lim} = 370$ MPa was reached at 5.4×10^7 cycles when extrapolating the SN curve with a crack originating on the surface or at 5.94×10^9 cycles when extrapolating the SN curve with a crack starting from very close to the surface or s/s, as shown in Figure 7. It can therefore be assumed that fatigue failure for S355JR+AR parent metal is unlikely when the stress is below 370 MPa and over 5.5 billion cycles have been accumulated. In the existing experimental batch of S355JR+AR parent metal, two samples were found as outliers, as they demonstrated two orders of magnitude longer fatigue life compared to the primary group (surface crack), so they have been grouped into a secondary s/s group with a corresponding SN curve in Figure 7.

The conventional fatigue limits at low frequency were found to be 210 MPa for S275JR+AR parent metal and 240 MPa for S355JR+AR parent metal according to the Table 2. Therefore, the quantitative difference between conventional and USF fatigue limits $\Delta\sigma_{lim}$ is found the same 130 MPa for both parent metals. However, the quantitative difference between 15-Hz and 20-kHz SN curves in terms of stress amplitude $\Delta\sigma_a$ was found not the same for these grades. For S275JR+AR parent metal, $\Delta\sigma_a$ was measured as 167.7 MPa on average, which varied from 178 MPa at 1.0×10^4 cycles to 154.6 MPa at 1.0×10^{10} cycles. For S355JR+AR parent metal, $\Delta\sigma_a$ was measured in terms of stress amplitude as 153.2 MPa on average, which varied from 134.1 MPa at 1.0×10^4 cycles to 163.5 MPa at 1.0×10^{10} cycles. This difference in stress amplitude $\Delta\sigma_a$ between 15-Hz and 20-kHz SN curves is apparently bigger for S275JR+AR compared to S355JR+AR parent metal (167.7 vs. 153.2 MPa correspondingly), which designates S275JR+AR grade as more strain-rate sensitive. The strain-rate sensitivity of S275JR+AR grade was

discussed in the preceding work [2] and determined to have a direct correlation with the volume content of ferrite.

It is commonly understood that there is a significant strain-rate sensitivity present in BCC materials, which is caused by the resistance to dislocation motion at higher strain rates [42]. As such, materials that contain large BCC regions, such as the ferrite phases present in carbon steels, tend to exhibit significant frequency effects which are caused by this strain-rate sensitivity [8–10, 43]. It been shown by Bach et al. [8] that for a range of carbon steels, the strain-rate sensitivity has a direct correlation with the volume content of ferrite. For steels with a greater ferrite content, a greater strain-rate sensitivity was observed, which leads to a greater discrepancy between the SN curves produced at US and at traditional frequencies. In order to evaluate the volume content of ferrite in the tested steels, image analysis was used on micrographs taken of the tested materials, following the procedures laid out in ASTM E1245-03 [44]. Sections were taken at a magnification of ×200 times from four random points in each material, and the results were averaged to mitigate the influence of material variability. For the S355JR+AR subgrade, ferrite content evaluation based on four samples (A—75.5%, B—78.3%, C—76.3% and D—75.0%) produced an average value of 76% (see Figure 8b), which is lower compared to 82% for S275JR+AR grade (see Figure 8a) also based on four samples (A—80.9%, B—81.1%, C—84.1% and D—83.1%). It can be seen that the parent metal containing 6% higher ferrite content (S275JR+AR) had a more significant discrepancy between the SN curves at the two test frequencies (8% higher); therefore, it had a higher strain-rate sensitivity. This agrees with the observations reported by Bach et al. [8] that a greater ferrite content correlates to a greater strain-rate sensitivity in the material.

5.2 | Weldments

Table 5 summarises the USF testing statistics of welded samples for S275JR+AR and S355JR+AR grades with different surface condition. Based on the corresponding illustrations of USF testing results for S275JR+AR welds shown in Figure 6 and S355JR+AR welds in Figure 7, it is obvious that the welding porosity has the defining detrimental effect on the fatigue life of weldments. An
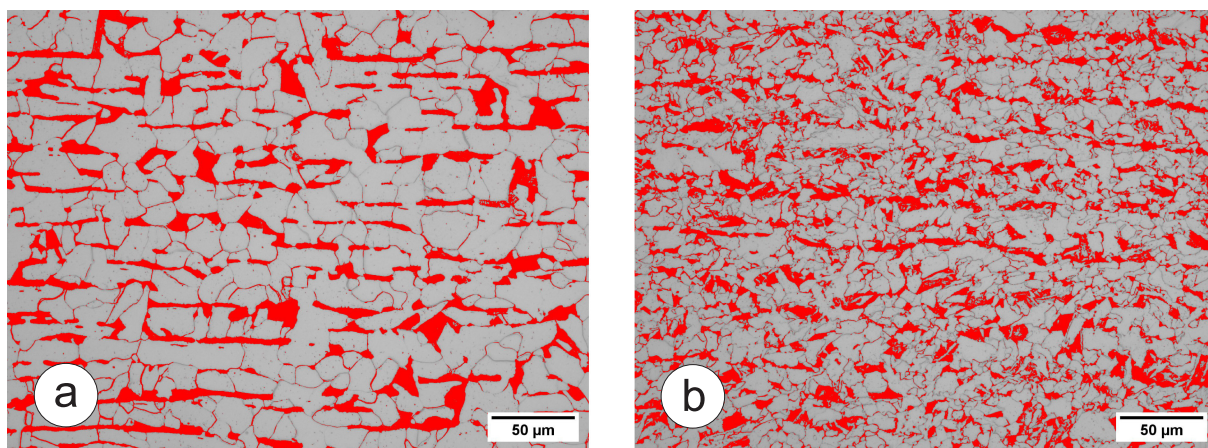
FIGURE 8 | Processed micrographs (×500) of S275JR+AR (a) and S355JR+AR (b) showing the pearlite highlight (red) and ferrite (grey) regions.

absolute majority of the weld samples have a fatigue life significantly lower than the parent material. Just a few samples for S275JR+AR welds tested in the stress range of 340–360 MPa surpass the parent SN curve with slightly longer fatigue life (see Figure 6), which can be explained by the absence of 'big and medium' pores and the location of the crack origin on the surface. A special group of welded samples made S275JR+AR tested in the stress range of 375–410 MPa surpasses the parent SN curve with notably longer fatigue life, as can be seen with blue and purple circles on the diagram in Figure 7. This group represents the samples selected using computed tomography (CT) scanning with the absence of 'big and medium' pores > 100 μm and the location of the crack origin on the surface. Blue circles represent the results with zero mean stress, corresponding to stress ratio $R = -1$. While purple circles represent the samples tested under tougher conditions with positive mean stress in the range of stress amplitudes σ_a from 376 to 420 MPa. A constant pretension of 1.5 kN equivalent to a constant component of tensile stress of 214.6 MPa was applied to those samples using Shimadzu AG-X series (AG-X5kN) frame, corresponding to the range of stress ratios R from −0.27 to −0.32. Even by adding a significant tensile component of stress, defect-free or 'almost' defect-free (with pores diameter < 100 μm) samples demonstrate the fatigue life comparable to the parent material SN curve. This experimental observation proves the assumption that elimination of the pores from the weld would make it as fatigue resistant as a parent material.

To study the effect of corrosion on the fatigue resistance of welds, four batches of precorroded samples have been prepared exactly in the same way as described in previous work [2]: S275JR+AR welds—6 samples precorroded for 2 weeks and 12 samples precorroded for 1 month; S355JR+AR welds—7 samples precorroded for 2 weeks and 11 samples precorroded for 1 month. The surface roughness of the precorroded samples was measured using the surface roughness machine Mitutoyo SV 600 and appeared to be $Ra = 12.5$ μm on average for the samples precorroded for 2 weeks, and $Ra = 15.5$ μm on average for the samples precorroded for 1 month, with a variation of ± 0.5 μm. An important observation is that detrimental effect of the corrosion on the fatigue life is stronger than the effect of welding porosity on the fatigue life, with a majority of the precorroded samples having a crack origin from a corrosion pit on the surface. The obtained fatigue data points for samples with polished (green triangles) and precorroded surface (orange and brawn diamonds) are scatted quite uniformly around the semi-logarithmic diagrams in Figure 6 for S275JR+AR welds and Figure 7 for S355JR+AR welds. This experimental observation proves the assumption of the random nature of damaging effects caused by both welding pores and corrosion pits. The damaging effect of corrosion pits over the time was measured using the surface roughness machine Mitutoyo SV 600 as reported in the preceding work [2].

There is a significant variation in both the size and location of pores which has a massive effect on the fatigue life of each welded sample. The size of pores that initiated the crack growth and resulted in failure varies from 50 μm to almost 1 mm, with a distance to the surface varying from the centre of the sample cross-section to a few micrometres or partly open pore. At the similar nominal stress amplitude level, the fatigue life can vary from 1 million cycles for a small s/s pore (see pore in Figure 9 with Ø = 75 μm) to 100 million cycles for a relatively big pore sitting away from the surface (see the pore in Figure 10 with Ø = 470 μm which is 640 μm away frow surface). Figure A7 of Appendix C show six S355JR+AR welded samples with optically measured pores that were the origin of crack initiation. Measuring the welding pores from the rest of the fractured samples is the first step to the development of the map of welding quality. By accurately quantifying and characterizing the welding pores, the valuable insights into the integrity and structural properties of the welded joints can be gained. This information serves as a crucial foundation for the subsequent stages of the welding defects map development process.

TABLE 5 | Number of tested weld samples.

Surface condition	S275	S355
Polished surface (with pores)	40	34
Polished surface (no pores)	5	10
Precorroded for 2 weeks	6	7
Precorroded for 1 month	12	13
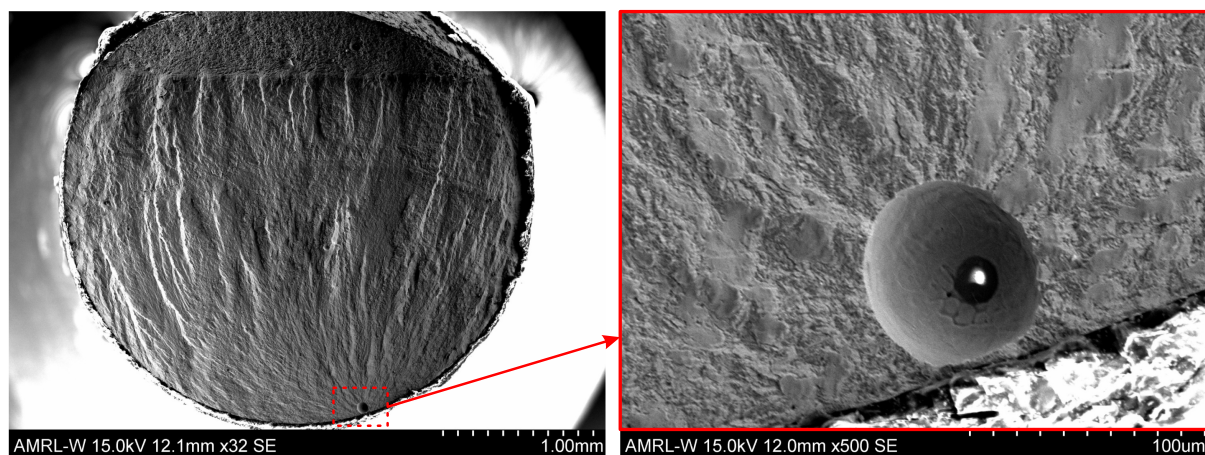
FIGURE 9 | Typical small welding pore with Ø = 75 μm found on fracture surfaces of USF testing specimens cut from weldments.
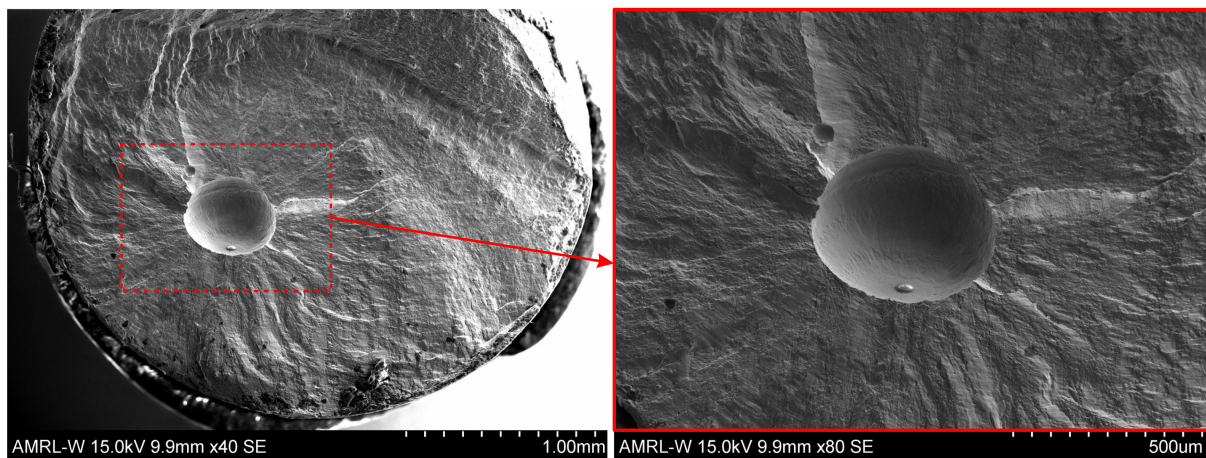
FIGURE 10 | Typical big welding pore with $\emptyset = 470\,\mu m$ which is $640\,\mu m$ away frow surface of USF testing specimens cut from weldments.
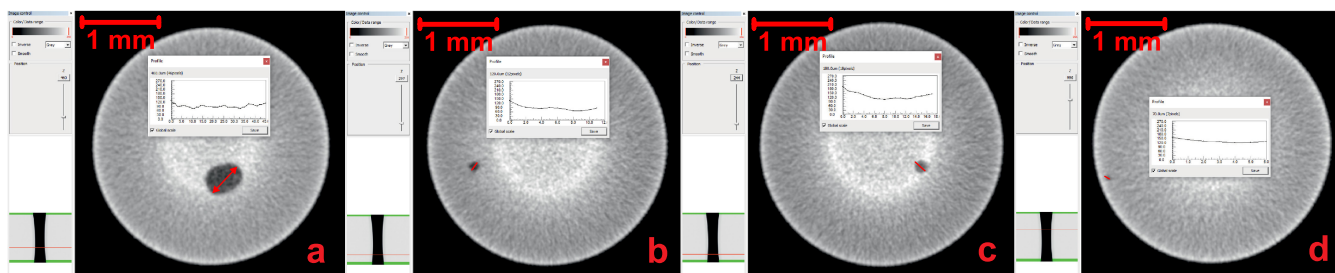
FIGURE 11 | Studying the welding pores displayed in 3D in Figure 14 via discrete cross-sections of Sample No. 37 made of S275JR+AR (duration of 166-m cycles at stress amplitude of 264 MPa) obtained with micro-CT scanning showing (a) big internal $\emptyset = 450\,\mu m$, (b) small internal $\emptyset = 120\,\mu m$, (c) medium internal $\emptyset = 180\,\mu m$ and (d) small subsurface $\emptyset = 70\,\mu m$.

The detrimental effect of welding porosity can be studied by measuring a detailed 3D topography using high-resolution X-ray micro-CT system—SkyScan 2211 from Bruker. X-ray micro-CT scanning technology was used to create a 3D map of pores in each sample including their relative location and size. It should be noted that CT scanning technique was used to study the samples with polished surface, which allows to recover not only the size of the critical pore but also its location that caused the fatigue failure of the sample. The 3D map created by CT scanning contains the statistical information and parameters of all the pores in each scanned sample with the resolution of $10\,\mu m$ in this research for the faster scanning. Understanding the mechanics of the crack initiation and propagation associated with the welding pores size and location is a key to the design of reliable and fatigue-resistant welded structures. The random character of the welding pores size and location is the best to be illustrated using the fracture surfaces of the tested samples—see Figures 9, A7 and 10.

Another example of the large variation of pore size and location can be demonstrated with CT scanning results obtained with DataViewer application from Bruker of two randomly picked samples cut from Plate ID No. ZL805 made of S275JR+AR shown in Figure 4. Figure 11 shows the cross-sections with pores in Sample No. 37 that lasted 166 million cycles at stress amplitude of $\sigma_a = 264\,MPa$. Crack in this sample has initiated on the big internal pore in Figure 11a with diameter of $\emptyset = 450\,\mu m$. On other hand, Figure 12 shows the cross-sections with pores in

Sample No. 45 that lasted 81.8 million cycles at stress amplitude of $\sigma_a = 239\,MPa$. Crack in this sample has initiated on the big open pore in Figure 12b with diameter of $\emptyset = 480\,\mu m$. Compared to Sample No. 37, Sample No. 45 has similar stress amplitude level (10% difference) and pore diameter (7% difference), but twice shorter fatigue life, as illustrated in Figure 6. This can be explained by fact that Sample No. 37 had both phases of crack initiation and crack propagation with internal crack front, while Sample No. 45 had only phase of crack propagation with external crack front.

Three samples cut from Plate ID No. ZL781 shown in Figure 4 were picked to examine the welding pores in S355JR+AR welded samples. Figure 13a shows the cross-section of one pore in Sample No. 6 that lasted 148 million cycles at stress amplitude of $\sigma_a = 330\,MPa$. Crack in this sample has initiated on the medium internal pore with diameter of $\emptyset = 300\,\mu m$. Very similarly, Figure 13b shows the cross-section of one pore in Sample No. 10 that lasted 137 million cycles at stress amplitude of $\sigma_a = 350\,MPa$. Crack in this sample has also initiated on the medium pore with diameter of $\emptyset = 250\,\mu m$. Comparing these two samples, they were tested at the similar stress levels with $\Delta = 6\%$, and they had a similar pore location and size with $\Delta = 16\%$ in diameter, that resulted in a similar fatigue life with $\Delta = 7\%$ in number of cycles, as can be seen in Figure 7. On other hand, Sample No. 12 with the cross-sections of two pores shown in Figure 13c,d lasted only 1.12 million cycles at much lower stress amplitude of $\sigma_a = 290\,MPa$. The whole reasons for a relatively short fatigue
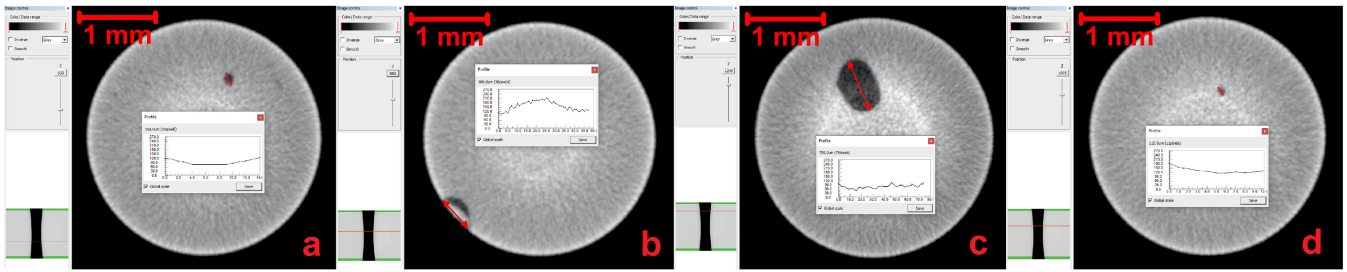
FIGURE 12 | Studying the welding pores displayed in 3D in Figure 14 via discrete cross-sections of Sample No. 45 made of S275JR+AR (duration of 81.8-m cycles at stress amplitude of 239 MPa) obtained with micro-CT scanning showing (a) small internal $\emptyset = 150\,\mu m$, (b) big open $\emptyset = 480\,\mu m$, (c) big internal $\emptyset = 750\,\mu m$ and (d) small internal $\emptyset = 110\,\mu m$.
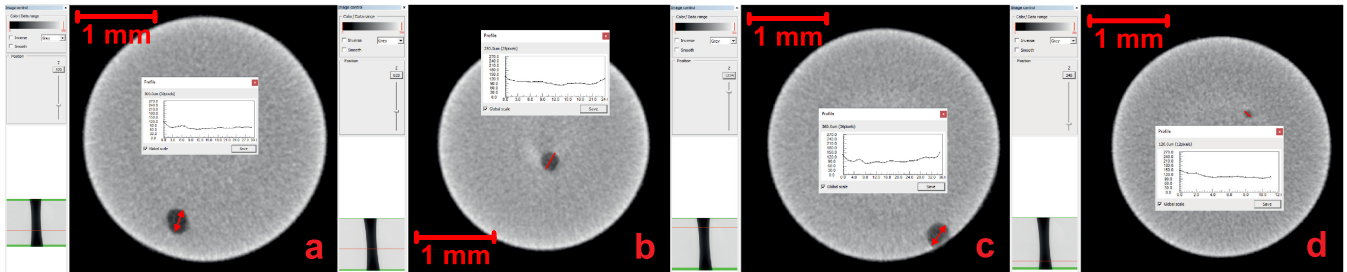
FIGURE 13 | Studying the welding pores displayed in 3D in Figure 14 via discrete cross-sections of samples made of S355JR+AR obtained with micro-CT scanning showing (a) medium internal $\emptyset = 300\,\mu m$ (Sample No. 6), (b) medium internal $\emptyset = 250\,\mu m$ (Sample No. 10), (c) big open $\emptyset = 360\,\mu m$ and (d) small internal $\emptyset = 120\,\mu m$ (both Sample No. 12).
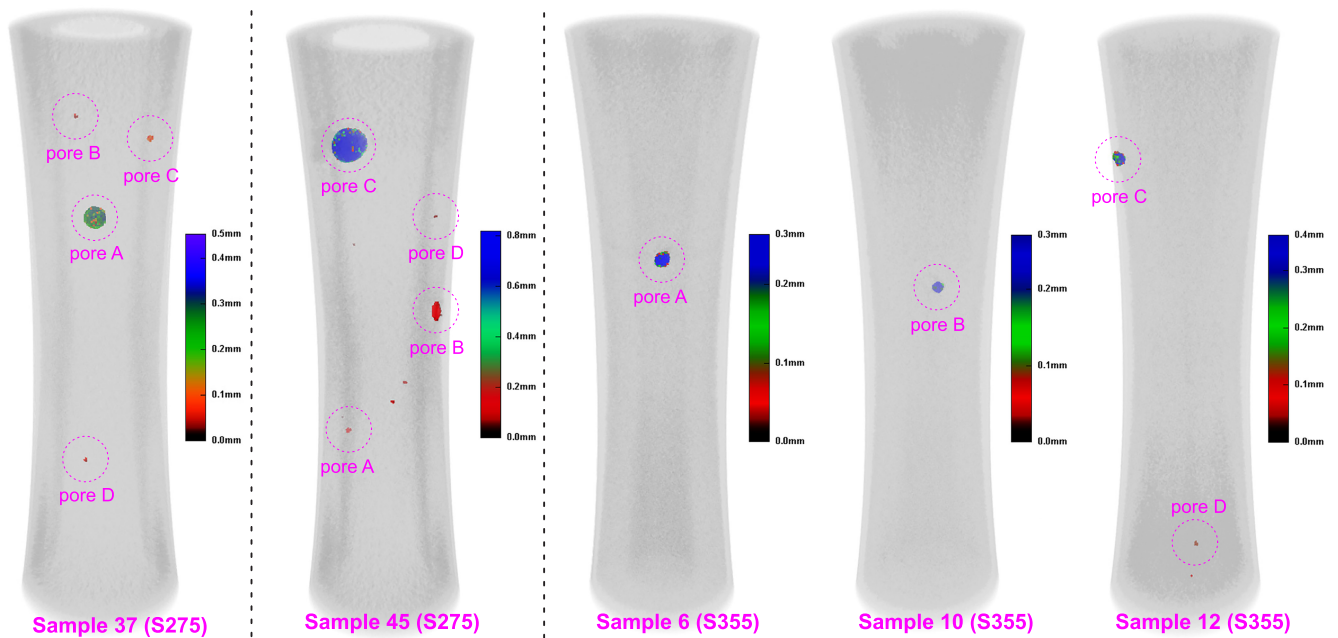
FIGURE 14 | Random character of the internal welding defects topology demonstrated with a rendered volume of welding pores using CTVox software from 3D micro-CT scans of USF testing Sample Nos. 37 (see Figure 11) and 45 (see Figure 12) made of S275JR+AR and Sample Nos. 6, 10 and 12 (see Figure 13) made of S355JR+AR grade.

life at low stress is a big open pore with a diameter of $\emptyset = 360\,\mu m$ shown in Figure 11c. It is a big surface defect and stress concentrator that triggers a fast crack growth without any crack initiation stage, that resulted in a quick sample failure, as illustrated in Figure 7.

An alternative and more informative way to visualise the welding pores is to use Bruker's 3D visualisation software CTVox for micro-CT volume rendering. The 3D maps of welding pores discussed above and shown in Figure 14 were obtained by the rendering separately of the metal volume of the sample and

internal/external voids in it. CT scanning resolution of 10 μm is enough to visualise the whole range of welding pores requited to be detected (diameter Ø from 50 to 1000 μm):

- *Small pores*: B, C and D in Sample No. 37; A and D in Sample No. 45 (both S275JR+AR); D in Sample No. 12 (S355JR+AR);

- *Medium pores:* A in Sample No. 6; B in Sample No. 10; C in Sample No. 12 (all S355JR+AR);

- *Big pores:* A in Sample No. 37; C in Sample No. 45 (both S275JR+AR);

- *Open pores:* B in Sample No. 45 (S275JR+AR); C in Sample No. 12 (S355JR+AR).

It should be noted that 3D rendering of welding pores volume is a convenient way to estimate a risk of quick fatigue failure of a sample. The 3D map of pores gives the information not only about the size of a pore but also on its relative location. This is critically important in case of very big pores, subsurface pore, but mostly for open pores, as can be seen on example of Sample No. 12 (shown in Figures 13c and 14) made of S355JR+AR grade with a very short fatigue life.

Summarising the visual and quantitative analysis of fatigue failures, the relation between welding pore (1) size, (2) location and (3) nominal stress and corresponding fatigue life is evidently direct. One would expect a notably shorter fatigue life from samples with big pores close to the surface or simply open pores even at low stresses. On other hand, the fatigue life of samples with smaller pores in the centre of sample quite often approach the SN curve of the parent metal. However, considering the amount of obtained experimental data, an individual approach to each pore for the purpose of nominal stress correction is not feasible at present stage of research. This would require a deeper analysis of the pore topology and evolution of the stress in the vicinity of the pore and planned for further investigation.

6 | Discussion

Visual comparison of fatigue data for S275JR+AR and S355JR+AR welded samples poses a notable challenge, because of the massive scatter of experimental data points. To address this issue in the analysis of experimental results, a fatigue performance parameter (FPP) (P_{fp}) is applied to the available experimental fatigue data to quantify the quality of the material in terms of fatigue resistance:

$$P_{fp} = \ln N \cdot \sigma_a, \qquad (2)$$

where N is a number of cycles to failure and σ_a is a nominal stress amplitude.

The FPP (P_{fp}) was applied to the experimental data for parent materials and for welded samples in different surface conditions (polished, precorroded for 2 weeks and precorroded for 1 month) to tackle the wide data scatter. The main results of data processing are shown in Table 6 with minimum, maximum, range and mean values of P_{fp} for all four variants of the material. It should be noted that the data scatter manifests itself in the range value, which is low for the parent materials, but it is three to four times higher for welded samples for all surface conditions.

Welds made of currently preferred steel S355JR+AR and the candidate steel S275JR+AR were tested at US frequency of 20 kHz in two conditions—polished surface and precorroded. Out of 45 polished welded samples made of S275JR as reported in Table 5, 40 samples (88%) have the crack initiated from pores in weld metal. Out of 44 polished welded samples made of S355JR as reported in Table 5, 34 samples (77%) have the crack initiated from pores in weld metal. The obtained experimental data were aggregated and processed using a FPP (P_{fp}) as mentioned above and reported in Table 6 (and illustrated in Figure 15) to identify a better performing grade. Comparison of P_{fp} for parent materials with polished surface demonstrated a significant advantage of 12.8% for S355JR+AR grade which is attributed to a higher yield strength resulting in a longer time to crack initiation. However, this advantage reduces to
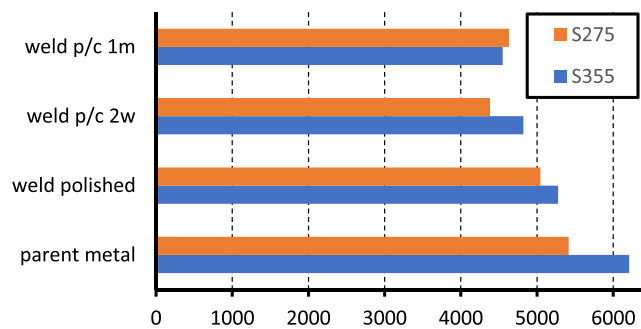
FIGURE 15 | Quantitative comparison of the fatigue performance parameter P_{fp} for different surface conditions of steel grades S275JR+AR and S355JR+AR according to Table 6.

TABLE 6 | Statistics of the fatigue performance parameter (P_{fp}) applied to the fatigue data for S275JR+AR and S355JR+AR grades.

	Grades	S275JR+AR				S355JR+AR				
	Values	Min.	Max.	Range	Mean	Min.	Max.	Range	Mean	Δ %
Surface condition	Parent polished	5122.9	5699.0	576.1	5415.4	5822.7	6586.8	764.1	6209.8	12.8%
	Weld polished	3064.6	6696.5	3631.9	5044.9	3912.2	6670.2	2758.0	5275.8	4.4%
	Weld p/c 2 weeks	3637.9	5169.6	1531.7	4382.1	4022.0	6063.9	2042.0	4820.3	9.1%
	Weld p/c 1 month	3189.4	5246.6	2057.2	4630.8	3361.5	5733.0	2371.5	4550.4	−1.8%

just 4.4% difference in P_{fp} for welded samples with polished surface, where the cracks mostly initiate from the welding pores. This observation proves that internal welding defects eliminate any benefits of higher yield strength by a sharp reduction of the time to crack initiation.

But the most important finding is that the comparison of welded samples in the 1-month precorroded condition shows a slight benefit of 1.8% for the candidate grade S275JR+AR. It should be noted that in precorroded samples the cracks mostly initiate from the corrosion pits on the surface rather than from pores, that proves a higher damaging effect of corrosion on the fatigue performance compared to the negative influence of porosity. The data for the 2-week precorroded condition does not show the benefit for the candidate grade S275JR+AR, it is still useful. Though the statistics of six samples for S275JR+AR welds and seven samples for S355JR+AR samples is not enough to make the useful conclusions, it shows that even with three samples having big open pores precorroded S275JR+AR welds are still fatigue resistant. The advantage of S275JR+AR precorroded welds can be associated with a higher ductility of this grade resulting in a longer time of the crack propagation. Theretofore, the major advantage of S275JR+AR welds is a better tolerance to both external defects (corrosion pitting) and internal defects (welding porosity). The influence of all other types of external defects (sharp geometry in weld toe and root) and internal defects (slag inclusion, incomplete fusion/penetration) on fatigue and their relation to ductility are investigated in the parallel research work [23].

7 | Conclusions

This paper reports outcomes of the research devoted to accelerated gigacycle fatigue testing at 20 kHz of the welds made of structural steels S275JR+AR and S355JR+AR. This research addressed the 'bottleneck' related to the conventional fatigue testing, which is unfeasible for test duration over 10 million cycles. The obtained results included two fatigue datasets for polished samples and fatigue datasets for precorroded samples (2 weeks and 1 month). All testing was implemented using USF testing system Shimadzu USF-2000A with tapered USF samples cut out of the welded plates. Fatigue testing was run at 20 kHz under zero mean stress condition $R = -1$ with a duration up to 1 billion cycles for most of samples. Statistical approach using a FPP (P_{fp}) was applied to highly scattered data points in order to comprehend the experimental results. As a main practical result, the advantage of S275JR+AR grade for precorroded welds was proved compared to S355JR+AR grade and associated with a higher ductility. Other important conclusions and observations that drawn from this research work are as follows:

- The advantage of welded structures made of S275JR+AR grade would be a better tolerance to both external and internal defects coming from the longer and slower crack growth stage.

- The detrimental effect of the corrosion on the fatigue life is stronger than the effect of welding porosity on the fatigue life, with a majority of the precorroded samples having a crack origin from a corrosion pit on the surface.

- Elimination of the pores from the weld or keeping the diameter of the pores under $\varnothing < 100\,\mu m$ and away from the surface of the welded structure would make it as fatigue resistant as a parent material.

- X-ray micro-CT scanning technology was used to create a 3D map of pores in each sample with the resolution of 10 μm in this research. It allowed to recover not only the size of the critical pores but also their location that may have caused the faster fatigue failure of the sample.

- The random character of the welding pores size and location can be illustrated using (1) fracture surfaces of the tested samples using SEM and optical microscopy, (2) cross-sections of USF testing samples obtained with micro-CT scanning and (3) 3D rendered volume of welding pores using CTVox software from 3D micro-CT scans of USF testing samples.

- 3D rendering of welding pores volume is a convenient way to estimate a risk of quick fatigue failure of a sample, as it gives the information not only about the size of a pore but also on its relative location.

- Visual and quantitative analysis of fatigue failures, the relation between welding pore (1) size, (2) location and (3) nominal stress and corresponding fatigue life is evidently direct. One would expect a notably shorter fatigue life from samples with big pores close to the surface or simply open pores even at low stresses.

- Understanding the mechanics of the crack initiation and propagation associated with the welding pores size and location is key to the design of reliable and fatigue-resistant welded structures.

The future work will focus on a detailed investigation on the welding defects including their morphology/distribution and the mechanisms of stress evolution in the vicinity of the pore and its effect on the fatigue performance. This will deliver a map of fail-safe welding pore sizes and locations for nominal stress conditions using available micro-CT scanning and fracture micrograph data from previous project and to evaluate a real stress in a vicinity of the pore for each fractured sample. Based on these data, the developed maps of welding pores will formulate the criteria of acceptance in the coordinates of pore diameter, pore proximity to surface and nominal stress.

Conflicts of Interest

The authors declare no conflicts of interest.

Data Availability Statement

Data are available on request from the authors.

References

1. EN 10025-2, *Hot Rolled Products of Structural Steels—Part 2: Technical Delivery Conditions for Non-Alloy Structural Steels* (European Committee for Standardization, 2019).

2. Y. Gorash, T. Comlekci, G. Styger, J. Kelly, F. Brownlie, and L. Milne, "Ultrasonic Fatigue Testing of Structural Steel S275JR+AR With Insights Into Corrosion, Mean Stress and Frequency Effects," *Materials* 16, no. 5 (2023): 1799.

3. L. Milne, Y. Gorash, T. Comlekci, and D. MacKenzie, "Frequency Effects in Ultrasonic Fatigue Testing (UFT) of Q355B Structural Steel," *Procedia Structural Integrity* 42 (2022): 623–630.

4. Shimadzu Corp., "USF-2000/USF-2000A Instruction Manual: Hardware," Shimadzu Corp., (2020), Manual v. 349-04408E.

5. J. Klusàk, V. Hornk, G. Lesiuk, and S. Seitl, "Comparison of High- and Low-Frequency Fatigue Properties of Structural Steels S355J0 and S355J2," *Fatigue & Fracture of Engineering Materials & Structures* 44, no. 11 (2021): 3202–3213.

6. P. Swacha and A. Lipski, "Cracking of S355J2+N Steel in the High-Cycle and Very-High-Cycle Fatigue Regimes," *International Journal of Fatigue* 168 (2023): 107388.

7. B. Guennec, A. Ueno, T. Sakai, M. Takanashi, and Y. Itabashi, "Effect of the Loading Frequency on Fatigue Properties of JIS S15C Low Carbon Steel and Some Discussions Based on Micro-Plasticity Behavior," *International Journal of Fatigue* 66 (2014): 29–38.

8. J. Bach, M. Göken, and H.-W. Höppel, "Fatigue of Low Alloyed Carbon Steels in the HCF/VHCF-Regimes," in *Fatigue of Materials at Very High Numbers of Loading Cycles*, ed. H.-J. Christ (Springer Fachmedien, 2018): 1–23.

9. N. Tsutsumi, Y. Murakami, and V. Doquet, "Effect of Test Frequency on Fatigue Strength of Low Carbon Steel," *Fatigue & Fracture of Engineering Materials & Structures* 32, no. 6 (2009): 473–483.

10. B. Guennec, T. Kinoshita, N. Horikawa, N. Oguma, and T. Sakai, "Loading Frequency Effect on the Fatigue Endurance of Structural Carbon Steels: Estimation Based on Dislocation Motion Theory and Experimental Verification of the Model," *International Journal of Fatigue* 172 (2023): 107634.

11. BS 7608, *Guide to Fatigue Design and Assessment of Steel Products* (BSI Group, 2014).

12. C. M. Sonsino, "Course of SN-Curves Especially in the High-Cycle Fatigue Regime With Regard to Component Design and Safety," *International Journal of Fatigue* 29, no. 12 (2007): 2246–2258.

13. X. Zhao, W. Dongpo, C. Deng, Y. Liu, and S. Zongxian, "The Fatigue Behaviors of Butt Welds Ground Flush in the Super-Long Life Regime," *International Journal of Fatigue* 36, no. 1 (2012): 1–8.

14. D. Yin, D. Wang, H. Jing, and L. Huo, "The Effects of Ultrasonic Peening Treatment on the Ultra-Long Life Fatigue Behavior of Welded Joints," *Materials & Design* 31, no. 7 (2010): 3299–3307.

15. C. He, Y. Liu, D. Fang, and Q. Wang, "Very High Cycle Fatigue Behavior of Bridge Steel Welded Joint," *Theoretical and Applied Mechanics Letters* 2, no. 3 (2012): 031010.

16. Y. Liu, C. He, C. Huang, M. K. Khan, and Q. Wang, "Very Long Life Fatigue Behaviors of 16Mn Steel and Welded Joint," *Structural Engineering and Mechanics* 52, no. 5 (2014): 889–901.

17. C. He, C. Huang, Y. Liu, and Q. Wang, "Fatigue Damage Evaluation of Low-Alloy Steel Welded Joints in Fusion Zone and Heat Affected Zone Based on Frequency Response Changes in Gigacycle Fatigue," *International Journal of Fatigue* 61 (2014): 297–303.

18. A. England, A. Toumpis, and Y. Gorash, "Very High Cycle Fatigue of Welds: A Review," *Metals* 13, no. 11 (2023): 1860.

19. P. R. Fry, "High Cycle Fatigue of Welded Structures: Design Guidelines Validated by Case Studies," *Engineering Failure Analysis* 46 (2014): 179–187.

20. F. Rumiche, A. Noriega, P. Lean, and C. Fosca, "Metallurgical Failure Analysis of a Welded Drive Beam of a Vibrating Screen," *Engineering Failure Analysis* 118 (2020): 104936.

21. J. Steyn, "Fatigue Failure of Deck Support Beams on a Vibrating Screen," *International Journal of Pressure Vessels and Piping* 61, no. 2 (1995): 315–327.

22. M. Zhang, H. Zhang, M. Li, L. Liu, and P. Wang, "Fatigue Behavior and Mechanism of Dog-Bone-Shaped Specimens of FV520B-I in a Very High Cycle Regime," *Fatigue & Fracture of Engineering Materials & Structures* 45, no. 12 (2022): 3658–3676.

23. A. England, A. Toumpis, and Y. Gorash, "Specimen Design for Gigacycle Fatigue Testing of Structural Steel Welded Joints," *Procedia Structural Integrity* 57 (2024): 494–501.

24. B. Xue, Y. Li, W. Yi, et al., "Biaxial Very High Cycle Fatigue Testing and Failure Mechanism of Welded Joints in Structural Steel Q345," *Crystals* 14, no. 10 (2024): 850.

25. M.-L. Zhu, L.-L. Liu, and F.-Z. Xuan, "Effect of Frequency on Very High Cycle Fatigue Behavior of a Low Strength Cr-Ni-Mo-V Steel Welded Joint," *International Journal of Fatigue* 77 (2015): 166–173.

26. M.-L. Zhu and F.-Z. Xuan, "Failure Mechanisms and Fatigue Strength Assessment of a Low Strength Cr-Ni-Mo-V Steel Welded Joint: Coupled Frequency and Size Effects," *Mechanics of Materials* 100 (2016): 198–208.

27. C. Bathias, "Coupling Effect of Plasticity, Thermal Dissipation and Metallurgical Stability in Ultrasonic Fatigue," *International Journal of Fatigue* 60 (2014): 18–22.

28. J.-T. Hu, R. Chen, G. Zhu, C. Wang, M.-L. Zhu, and F.-Z. Xuan, "Heat Dissipation Behavior of a Low-Strength-Steel Welded Joint in Ultrasonic Fatigue," *Metals* 12, no. 11 (2022): 1857.

29. H. Yeom, B. Choi, T. Seol, M. Lee, and Y. Jeon, "Very High Cycle Fatigue of Butt-Welded High-Strength Steel Plate," *Metals* 7, no. 3 (2017): 103.

30. P. Wang, W. Wang, M. Zhang, Q. Zhou, and Z. Gao, "Effects of Specimen Size and Welded Joints on the Very High Cycle Fatigue Properties of Compressor Blade Steel KMN-I," *Coatings* 11, no. 10 (2021): 1244.

31. Z. Xiong, E. Peng, L. Zeng, and Q. Xu, "Giga-Cycle Fatigue Behavior of the Nuclear Structure of 316L Weldments," *Frontiers in Energy Research* 9 (2021): 696608.

32. M. Zhang, W. Wang, P. Wang, Y. Liu, and J. Li, "Fatigue Behavior and Mechanism of FV520B-I Welding Seams in a Very High Cycle Regime," *International Journal of Fatigue* 87 (2016): 22–37.

33. F. Liu, H. Zhang, H. Liu, et al., "Influence of Welded Pores on Very Long-Life Fatigue Failure of the Electron Beam Welding Joint of TC17 Titanium Alloy," *Materials* 12, no. 11 (2019): 1825.

34. WES 1112, *Standard Test Method for Ultrasonic Fatigue Testing of Metallic Materials* (Japan Welding Engineering Society, 2017).

35. Y. Furuya, Y. Shimamura, M. Takanashi, and T. Ogawa, "Standardization of an Ultrasonic Fatigue Testing Method in Japan," *Fatigue & Fracture of Engineering Materials & Structures* 45, no. 8 (2022): 2415–2420.

36. EN 1993-1-1, *Eurocode 3: Design of Steel Structures—Part 1-1: General Rules and Rules for Buildings* (European Committee for Standardization, 2005).

37. ASTM E466-21, *Standard Practice for Conducting Force Controlled Constant Amplitude Axial Fatigue Tests of Metallic Materials* (ASTM International, 2021).

38. ANSYS Inc., "GRANTA EduPack," Granta Design Ltd., (2020), Material Properties Database v. 20.1.0.

39. E. Haibach, *FKM-Guideline: Analytical Strength Assessment of Components in Mechanical Engineering*, 5th ed. (VDMA Verlag, 2003).

40. O. Basquin, "The Exponential Law of Endurance Tests," *Proceeding ASTM* 10, no. II (1910): 625–630.

41. ISO 5817, *Welding—Fusion-Welded Joints in Steel, Nickel, Titanium and Their Alloys—Quality Levels for Imperfections* (International Organization for Standardization, 2014).

42. H. Mughrabi, K. Herz, and X. Stark, "Cyclic Deformation and Fatigue Behaviour of α-Iron Mono- and Polycrystals," *International Journal of Fracture* 17, no. 2 (1981): 1573–2673.

43. I. Nonaka, S. Setowaki, and Y. Ichikawa, "Effect of Load Frequency on High Cycle Fatigue Strength of Bullet Train Axle Steel," *International Journal of Fatigue* 60 (2014): 43–47.

44. ASTM E1245-03, *Standard Practice for Determining the Inclusion or Second-Phase Constituent Content of Metals by Automatic Image Analysis* (ASTM International, 2016).

Appendix A

Drawings of USF Testing Samples
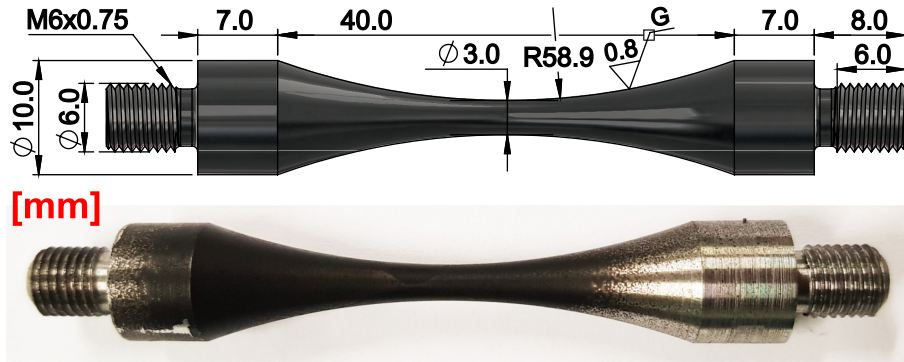
FIGURE A1 | Dimensions of USF sample (mm) and corresponding photo or a painted sample.

Appendix B

Welds Microstructure, Vickers Hardness and PWHT

Appendix C

Fracture Surfaces of Welded Samples
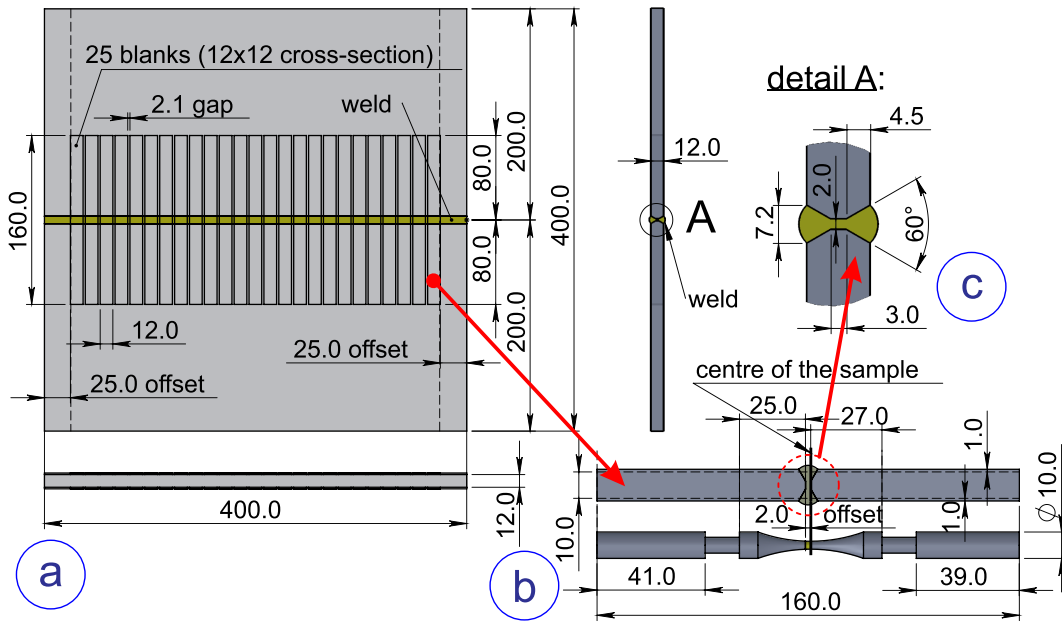
FIGURE A2 | Cutting of blanks and machining of USF samples from welded plates made of S275JR+AR grade with 12-mm thickness.
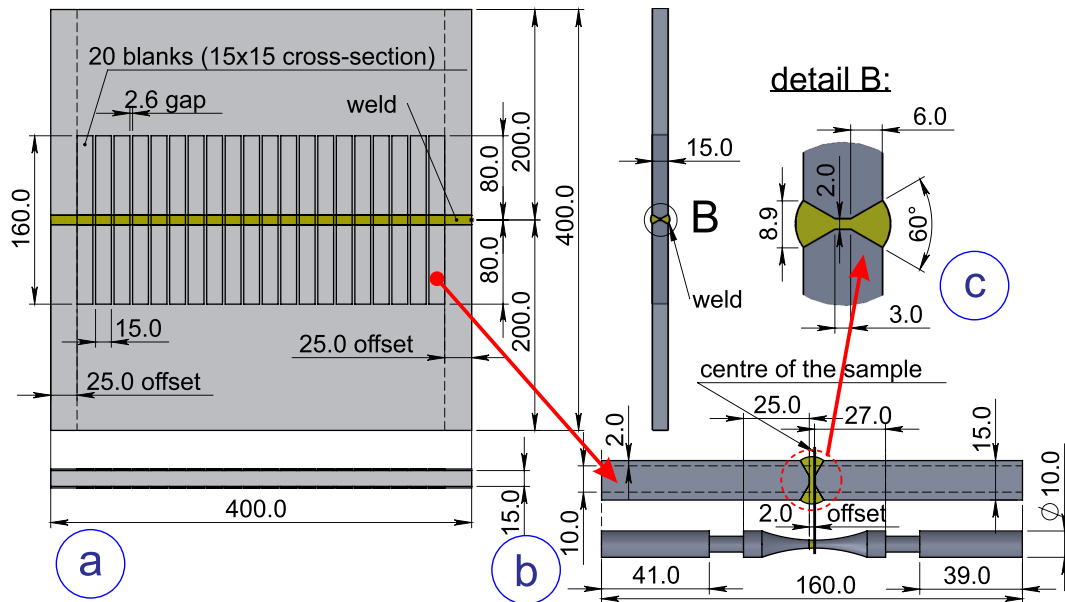
FIGURE A3 | Cutting of blanks and machining of USF samples from welded plates made of S355JR+AR grade with 15-mm thickness.
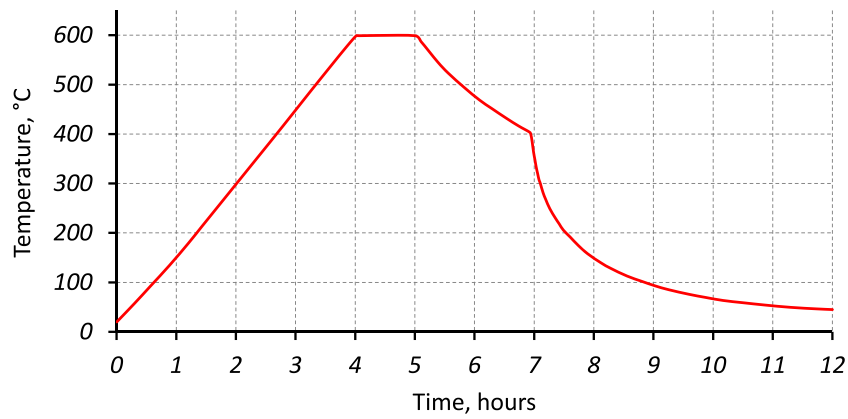
FIGURE A4 | Thermal history of postweld heat treatment (PWHT) for the welded USF testing samples.
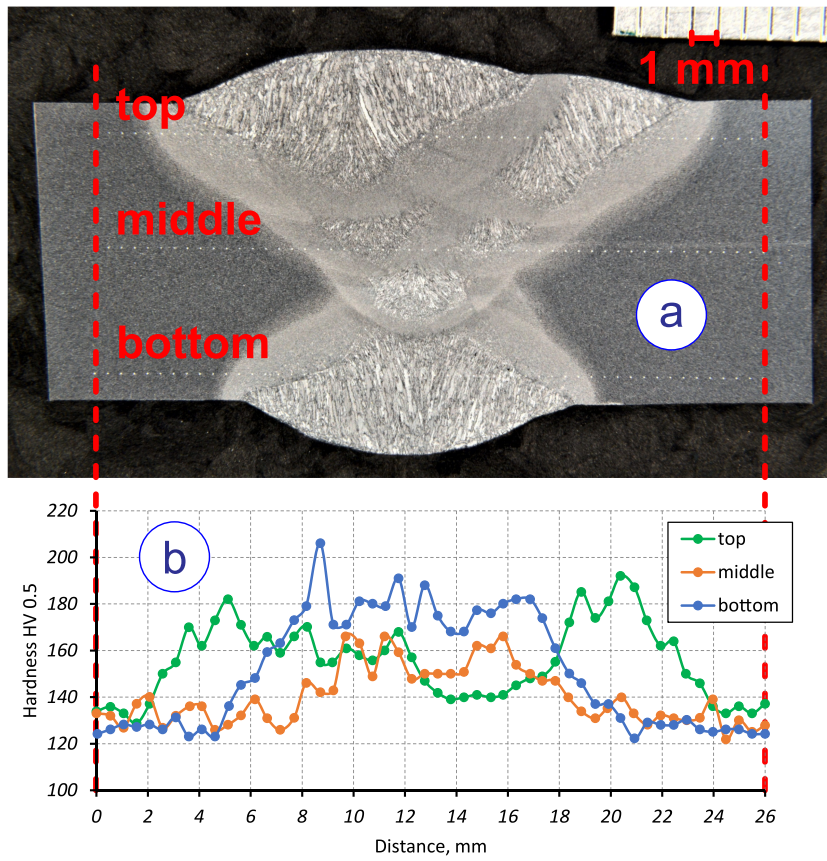
FIGURE A5 | Analysis of S275JR+AR weldment: (a) microstructure of full weld polished section and (b) Vickers hardness test *HV* 0.5 taken at different paths.
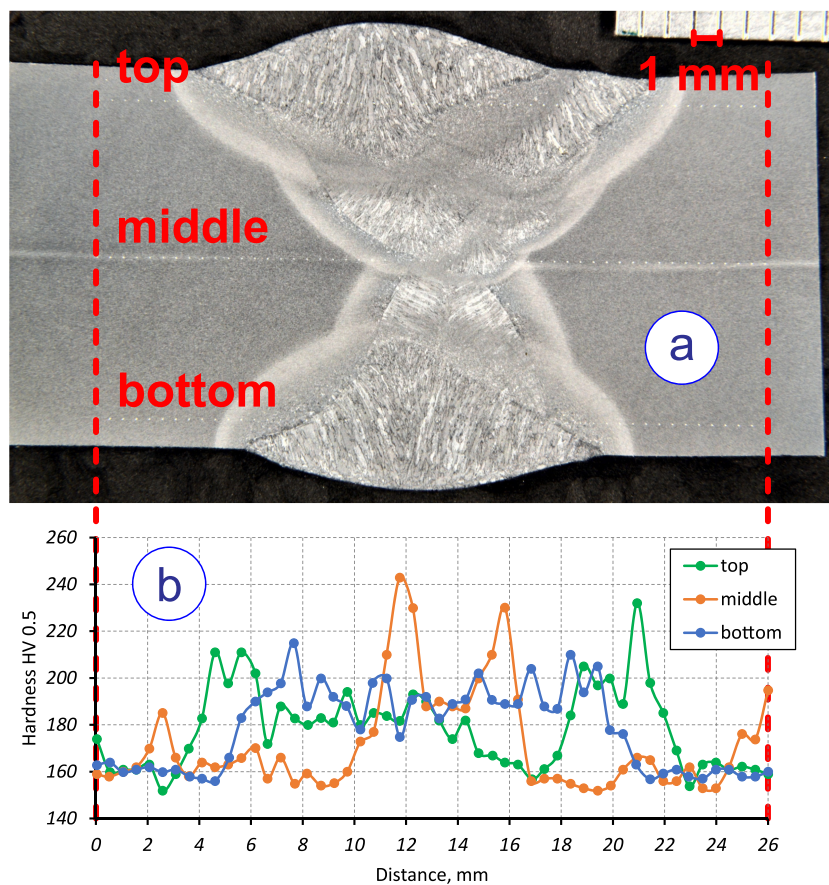
FIGURE A6 | Analysis of S355JR+AR weldment: (a) microstructure of full weld polished section and (b) Vickers hardness test *HV* 0.5 taken at different paths.
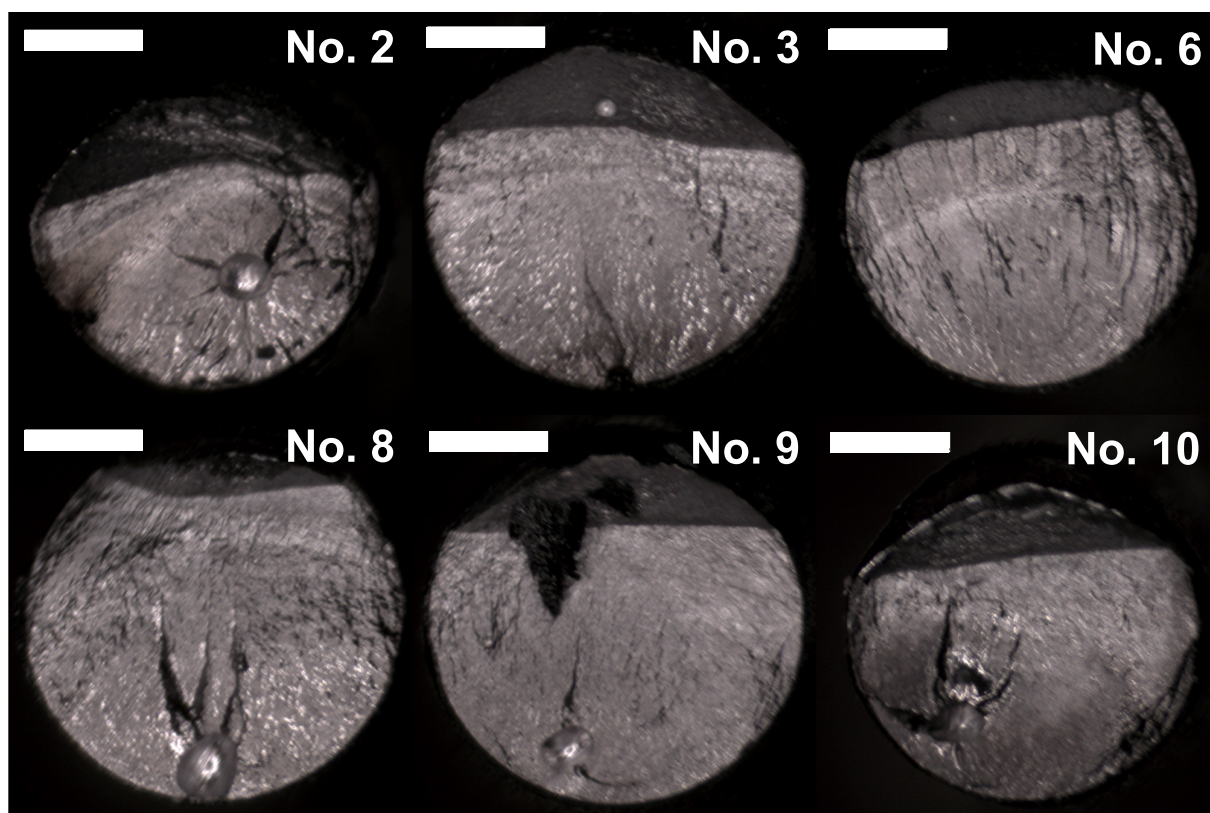
FIGURE A7 | Fracture surfaces of S355JR+AR welded samples with optically measured pores obtained with Yenway optical stereomicroscope.